ARCHIVES OF ELECTRICAL ENGINEERING **VOL. X(Y), pp. 1-25 (2026)**

This paper has been accepted for publication in the AEE journal. This is the version, which has not been fully edited and content may change prior to final publication.
Citation information: DOI 10.24425/aee.2026.156806

Multi-objective optimization for dynamic performance of overhead conductor rail anchor segments based on non-dominated sorting genetic algorithm II

XIA ZHAO[1], ZHULIN ZHANG[1*], YING WANG[1], XIUQING MU[1], LEIJIAO GE[2], MING TENG[3]

[1]*School of Automation and Electrical Engineering, Lanzhou Jiaotong University*
Lanzhou, 730070, China

[2]*School of Electrical and Information Engineering, Tianjin University*
Tianjin, 300072, China

[3]*Lanzhou Railway Bureau*
Lanzhou, 730015,China
e-mail:{zzlin19/19838025269}@163.com,
{2314486731/2568607[illegible]01/[illegible]336721984/2958047615}@qq.com

Abstract: The overlapping part between the overhead conductor rail (OCR) anchor segments is called the anchor joint, which is a key component that constrains the dynamic performance of the OCR. When the train passes through the anchor joint, the contact force fluctuates significantly, degrading the current collection quality. This paper carries out the multi-objective optimization of the dynamic performance at the OCR anchor segments by combining the Non-dominated Sorting Genetic Algorithm II (NSGA-II) with the Response Surface Method (RSM), in order to alleviate the severe fluctuations in contact force, thus making a trade-off between the two inconsistent objectives of contact force standard deviation (F_δ) and range (F_r). Firstly, the Box-Behnken experimental design method was employed, with the elevation of the first suspension point, cantilever span, anchor joint, and standard span as design variables, and F_δ and F_r as objective functions, to conduct numerical simulation studies on them. Secondly, to enhance the dynamic performance of OCR anchor segments, the NSGA-II was used to optimize the objective functions F_δ and F_r Finally, simulations using the geometric parameters corresponding to the Pareto optimal solutions obtained by the NSGA-II showed that, compared to the original design, F_δ was increased by 11.18%, and F_r was raised by 35.04%.

This paper has been accepted for publication in the AEE journal. This is the version, which has not been fully edited and content may change prior to final publication.
Citation information: DOI 10.24425/aee.2026.156806

Key words: anchor joint, contact force, multi-objective optimization, NSGA-II, response surface method

1. Introduction

In electrified railways, stable current collection from the pantograph and overhead conductor rail (POCR) is one of the key factors to ensure the stable operation of trains. During train operation, the complex vibration conditions of the pantograph and overhead conductor rail system (POCRS) cause the contact force to fluctuate continuously and complexly. Excessive or insufficient contact force can significantly affect the quality of current collection for the train. Especially at the anchor joint of the OCR, as shown in Fig. 1, the contact force fluctuates significantly, and its structure has an important impact on F[illegible] and F_r between the POCR. Excessive contact force here can lead to wear and disconnection between the POCRS, causing arcing and affecting the stable current collection for the train.

Fig. 1. The anchor section of OCR in the tunnel (left) and its local structure (right)

In recent years, most studies have focused on modeling the OCR and assessing how its parameters affect the dynamics of the POCRS. Because the OCR is structurally and functionally similar to the soft catenary[1], modeling approaches developed for the latter, especially the finite element method (FEM), which are readily transferable [2, 3]. For example, [4] developed an OCR FEM in ANSYS with a new conductor rail profile. [5] used the absolute nodal coordinate formulation (ANCF) to model the OCR and investigate pantograph catenary coupled dynamics, and [6] examined the influence of support stiffness on current collection quality. Reference [7] identified OCR irregularities caused by long-term undulating wear of the sliding surface and installation errors, as a major source of degradation. Structurally, early busbar forms are documented in [8], while modern OCR typically adopt hollow π-shaped sections for enhanced

This paper has been accepted for publication in the AEE journal. This is the version, which has not been fully edited and content may change prior to final publication.
Citation information: DOI 10.24425/aee.2026.156806

performance [9]. In addition, [10, 11] conducted systematic studies of pantograph catenary dynamics in the overlap region of soft catenaries, and [12] analyzed the effects of OCR parameters on POCRS dynamics. Overall, these studies are largely single-factor or classical experimental designs and do not account for multi-parameter coupling.

Given the pronounced coupling and synergy among OCR parameters, single-factor analyses are both inefficient and inadequate for accurate optimization. Although multi-objective swarm intelligence algorithms are still uncommon in the POCRS domain, they have been rigorously validated in related engineering fields, for instance, the breeder genetic algorithm (BGA) for multi-scenario DG siting and sizing to minimize distribution-network power loss [13], the salp swarm algorithm (SSA) for constrained optimization of outer-rotor BLDC motors with superior efficiency and solution quality [14], and an improved grey wolf optimizer (GWO) for transformer fault warning and classification with strengthened global search [15]. These results provide strong evidence for the applicability and reliability of such methods to POCRS problems.

This study targets the dynamic optimization of the OCR anchor segment. Using the elevation of the first suspension point, cantilever span, anchor joint parameter, and standard span as design variables, and F_δ and F_r as performance objectives, we conduct Box–Behnken design [16] based simulations of the POCRS contact force at the anchor joint and build a RSM surrogate that explicitly captures factor interactions. Based on this surrogate, the NSGA-II is employed to solve a strongly coupled, nonconvex, and constrained multi-objective problem, yielding the Pareto front of dynamic performance at the anchor joint and an optimal parameter set that suppresses contact force fluctuation, reduces separation risk, and enhances current collection stability.

2. Model description and computational method

2.1. The anchor segment geometric model of overhead conductor rail

The anchor joint of the OCR is divided into breakaway-type anchor joints and through-type anchor joints. This paper analyzes the breakaway-type anchor joint. It is realized by utilizing the geometric arrangement of two overlapping OCR segments, where the overlapping area has an equal high point in space, and the end of the anchor segment is elevated. The OCR anchor segment consists of the elevation of the first suspension point, cantilever span, the first span, and the second span. The arrangement of the anchor joint is shown in Figs. 2(a) and (b). In this paper, the elevation of the first suspension point x_1 is 4 mm, the cantilever span x_2 is 1.2 m, the first span L_1 is 2 m, the second span L_2 is 6 m, the transition span L_3 is 7 m, the anchor joint x_3 is 5.4 m, and the standard span x_4 is 10 m. Due to the large span of the first span, only the first suspension point is elevated.

This paper has been accepted for publication in the AEE journal. This is the version, which has not been fully edited and content may change prior to final publication.
Citation information: DOI 10.24425/aee.2026.156806

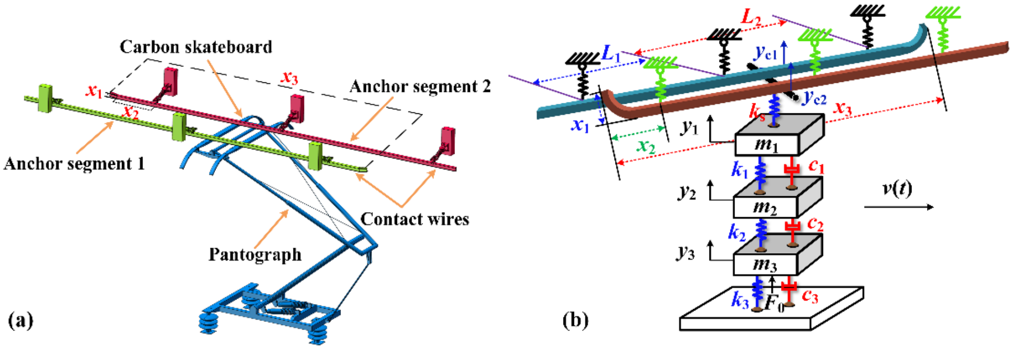

Fig. 2. The anchor segment model of overhead conductor rail under the action of the pantograph: (a) represents the actual model; (b) this lumped mass model can represent the actual model

2.2. Mathematical model and computational method

In this paper, the mathematical model involves two types of models: the pantograph and the overhead conductor rail. The pantograph model uses a three-mass model, while the OCR is regarded as a simply supported beam model. Table 1 [11] shows the parameters of the pantograph model. By coupling the two models via a penalty function [11], establish the equations of motion for the POCR coupled system, and on this basis construct Objective Functions F_δ [17] and F_r [18]. The analysis focuses on F_δ and F_r between the POCRS at the anchor segment under the influence of the pantograph. The POCRS at the anchor joint is illustrated in Fig. 2(a).

F_δ is mainly derived from the industry standard [17]; according to the standards, the requirement is $\delta \leq 0.3F_m$; therefore, we define

$$F_\delta = 0.3F_m - \delta. \tag{1}$$

In the equation, F_m represents the average contact force, and δ represents the standard deviation of the contact force.

$$\delta = \sqrt{\frac{1}{n}\sum_{i=1}^{n}(F_c - F_m)^2}, \tag{2}$$

where n represents the number of contact force data points and F_c denotes the contact force between the POCRS at the anchor segment.

F_r is also derived from the industry standard for assessing disconnection and wear between the pantograph and the overhead conductor rail [18].

$$F_r = 300 - (F_{\max} - F_{\min}), \tag{3}$$

where $F_{\max}$ represents the maximum contact force, and $F_{\min}$ represents the minimum contact force.

Table 1. Parameters of pantograph model

Dof	***m* (kg)**	***c* (N·s/m)**	***k* (N/m)**
1	6.1	10	10400
2	10.1	0	10600
3	10.3	120	0

The contact force between the POCRS at the anchor segment is

$$F_c = \alpha \cdot k_s(y_1 - y_{c1}) + \beta \cdot k_s(y_1 - y_{c2}). \tag{4}$$

In the formula, k_s represents the contact stiffness between the POCRS, y_1 represents the displacement of the pantograph head, and y_{cj} represents the displacement of the j-th contact wire, α is the weighting coefficient of the first contact wire, and β is the weighting coefficient of the second contact wire. Their expressions are as follows:

$$y_1 = \frac{F_t}{K_t}, \tag{5}$$

$$y_{cj} = \sum_{i=1}^{N} q_i \cdot \sin\left(\frac{i\pi vt}{x_3}\right) - x_1 \cdot \cos\left(\frac{\pi x_3 t}{2v}\right), \tag{6}$$

where: F_t represents the payload vector, K_t represents the payload matrix, N denotes the mode number of the overhead conductor rail vibration, q_i is the generalized vibration mode coordinate of the OCR, v is the train operating speed, t is the running time, x_1 is the elevation of the first suspension point, x_3 is the length of the anchor joint, and the anchor joint x_3 is composed of the cantilever span x_2, the first span L_1, and the second span L_2.

The contact force F_c between the POCRS is derived from the coupled motion differential equations of the overhead conductor rail and the pantograph, using the simply supported beam mechanical model shown in Fig. 2. Under the action of the pantograph, the motion differential equation of the overhead conductor rail is [19]

$$EI\frac{\partial^4 y}{\partial x^4} + \rho\frac{\partial^2 y}{\partial t^2} + c\frac{\partial y}{\partial t} = \delta(x - Vt)\{K_s[y_1 - y(x,t)]\}. \tag{7}$$

Using the modal decomposition method, substitute $y(x,t) = \sum_{i=1}^{\infty} q_i(t)\,\phi_i(x)$ into the above equation, multiply each term by the n mode-shape function $\phi_n(x)$, integrate over the entire length of the OCR, and, accounting for the orthogonality of the mode shapes, simplify to obtain

$$EIq_n(t)\int_0^L \phi_n(x)\frac{\mathrm{d}^4\phi_n(x)}{\mathrm{d}x^4}\mathrm{d}x+\rho\frac{d^2q_n(t)}{dt^2}\int_0^L \phi_n^2(x)\mathrm{d}x+c\frac{\mathrm{d}q_n(t)}{\mathrm{d}t}\int_0^L \phi_n^2(x)\mathrm{d}x$$

$$=\int_0^t \delta(X-Vt)[K_s y_1-K_s\sum_{i=1}^{\infty} q_i(t)\phi_i(x)]\phi_n(x)\mathrm{d}x. \tag{8}$$

For a conductor rail with a uniform cross-section, we can likewise assume $\phi_n(x)=\sin\frac{n\pi x}{L}$, with $x = vt$; substituting these into above equation, we get

$$\ddot{q}_n(t)+2\xi_n w_n\dot{q}_n(t)+w_n^2 q_n(t)+\frac{2}{\rho L}k_s\sum_{i=1}^{\infty} q_i(t)\sin\left(\frac{i\pi vt}{L}\right)\sin\left(\frac{n\pi vt}{L}\right)-\frac{2}{\rho L}k_s y_1\sin\left(\frac{n\pi vt}{L}\right)=0. \tag{9}$$

In this equation, q_i(t) represents the generalized vibration mode coordinates of the beam, which is a function of time *t*; $w_n=\frac{n^2\pi^2}{L^2}\sqrt{\frac{EI}{\rho}}$ is the *n*-th order frequency of the busbar, $c=2\xi_n w_n$ is the damping of the n-th mode, *EI* is the flexural rigidity, ρ is the linear density, and *L* is the length of the entire OCR anchor segment.

Here $n = 1-\infty$, the above equation has an infinite number of variables, and they are not independent of each other. When the displacement series is taken to *N* terms, the degrees of freedom can be simplified from an infinite number to *N*. The motion equation of the OCR can be represented in an *N*-th order matrix form.

$$[\boldsymbol{M}]\{\ddot{\boldsymbol{q}}\}+[\boldsymbol{C}]\{\dot{\boldsymbol{q}}\}+[\boldsymbol{K}]\{\boldsymbol{q}\}=\boldsymbol{F_c}. \tag{10}$$

Among them, ***M***, ***C*** and ***K*** are the generalized mass, damping and stiffness matrices, respectively, F_c denotes the POCRS contact force and is the generalized displacement vector of overhead conductor rail, and $\{\boldsymbol{q}\} = [q_1, q_2,\ldots, q_N]$.

The differential equation of motion for the pantograph is

$$\begin{cases} m_1\ddot{y}_1-c_1(\dot{y}_2-\dot{y}_1)-k_1(y_2-y_1)=-F_c \\ m_2\ddot{y}_2+(c_1+c_2)\dot{y}_2-c_1\dot{y}_1-c_2\dot{y}_3+(k_1+k_2)y_2-k_1y_1-k_2y_3=0. \\ m_3\ddot{y}_3+(c_2+c_3)\dot{y}_3-c_2\dot{y}_2+(k_2+k_3)y_3-k_2y_2=F_0 \end{cases} \tag{11}$$

In the equation, $\ddot{y}_1$, $\ddot{y}_2$, and $\ddot{y}_3$ represent the accelerations of the pantograph head, upper frame, and lower frame, respectively. $\dot{y}_1$, $\dot{y}_2$, and $\dot{y}_3$ denote the velocities of the pantograph head, upper frame, and lower frame, respectively. y_1, y_2, and y_3 are the displacements of the pantograph head, upper frame, and lower frame, respectively, and their schematic diagram is shown in Fig. 2(b). F_0 is the static lifting force applied to the lower frame of the pantograph.

2.3. Verification of model simulation

To demonstrate the effectiveness of the model, EN50367 [17] is primarily used as a reference, but the current standard does not provide a reference model for the coupling of the POCRS. In this paper, measurement data obtained from Lanzhou–Xinjiang Railway are used to verify the accuracy of the model. The parameters of the POCRS are shown in Tables 1 and 2, respectively, and the model of the OCR is established based on the aforementioned methods.

Figure 3(a)presents a comparison of the distance-contact force between simulated data and measured data. Figure 3(b) shows the maximum (Max), minimum (Min), average (Ave), and standard deviation (Std) of the contact force.

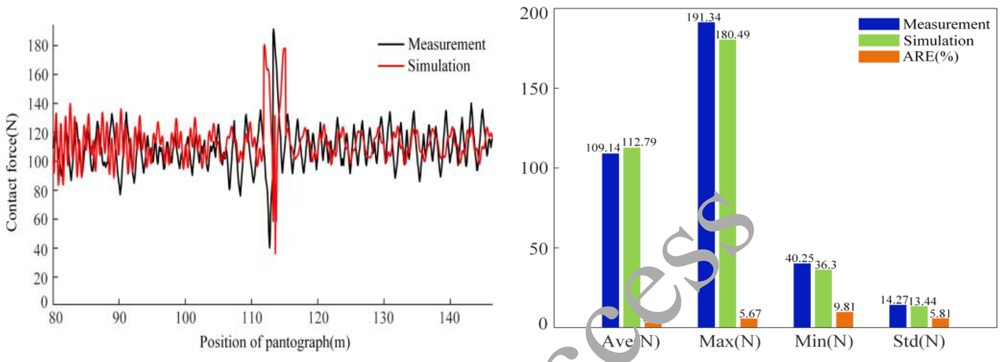

(a) (b)

Fig. 3. (a) Contact force of numerical simulation and measurement; (b) statistical comparison between measurement and simulation data

Table 2. Parameters of the OCR model

Span number	Span length (m)	Support stiffness (N/m)	Tensile stiffness (N/m)	Bending stiffness (N·m^2)
27	10	6.7×10^7	2.1×10^8	1.7×10^5

It is observed that the absolute relative errors (ARE) of the maximum, average, and standard deviation of the contact force are all within 6% of the measured data. All metrics are well below the 20% threshold specified in EN 50367, thereby verifying the reliability of the aforementioned model.

2.4. Influence of head lateral characteristics on POCRS dynamics

Considering lateral inclination, the equations of motion of the pantograph are

$$\begin{cases} J_\varphi \ddot{\varphi} + c_\varphi \dot{\varphi} + k_\varphi \varphi = M_c \\ m_1 \ddot{y}_1 - c_1(\dot{y}_2 - \dot{y}_1) - k_1(y_2 - y_1) = -F_c \\ m_2 \ddot{y}_2 + (c_1 + c_2)\dot{y}_2 - c_1 \dot{y}_1 - c_2 \dot{y}_3 + (k_1 + k_2) y_2 - k_1 y_1 - k_2 y_3 = 0 \\ m_3 \ddot{y}_3 + (c_2 + c_3)\dot{y}_3 - c_2 \dot{y}_2 + (k_2 + k_3) y_3 - k_2 y_2 = F_0 \end{cases} \quad (12)$$

This paper has been accepted for publication in the AEE journal. This is the version, which has not been fully edited and content may change prior to final publication.
Citation information: DOI 10.24425/aee.2026.156806

Among them, φ, $\dot{\varphi}$, and $\ddot{\varphi}$ illustrate the pantograph head lateral inclination angle, angular velocity, and angular acceleration. J_{φ}, c_{φ}, k_{φ} indicate the moment of inertia about the lateral-inclination axis, rotational damping, and rotational stiffness. Furthermore, it is coupled with Eq. (9) of the OCR equations of motion via the penalty function to perform numerical simulations and obtain the results, as shown in Fig. 4.

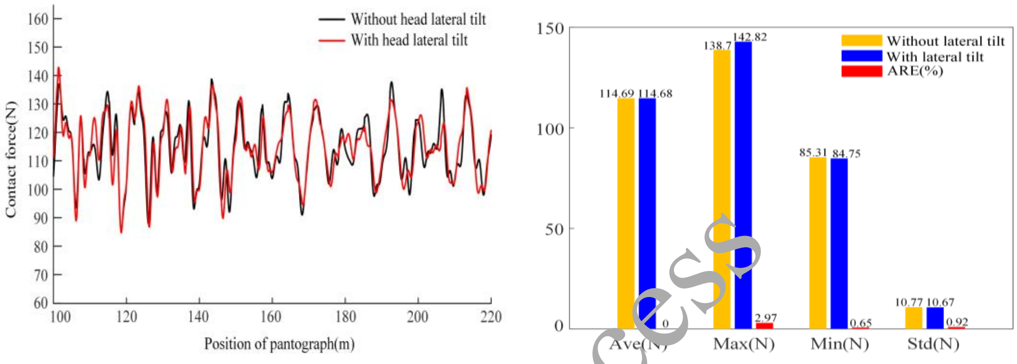

(a) (b)

Fig. 4. (a) Contact force without tilt and with tilt, (b) statistical comparison between without tilt and with tilt

From Fig. 4(a), the contact force waveforms with and without lateral inclination of the pantograph head nearly coincide, demonstrating that the lateral inclination has a negligible effect on the POCRS contact force. As shown by the statistics in Fig. 4(b), the average (AVE) contact force is almost identical in the two cases, the maximum absolute relative error (ARE) is 2.97%, and all absolute relative errors of the “with inclination” case relative to the “without inclination” case are within 3%. This further confirms that the model without pantograph head lateral inclination is also reasonably accurate. Therefore, the effect of the pantograph head’s lateral tilt angle is not considered in the subsequent analyses of this paper.

Additionally, regarding the horizontal distance, we assume that the horizontal spacing between the two OCR at the overlap joint is d, within our point-contact framework, as previously indicated, the contact force F_c is given by Eq. (4). The contact force Fc is only related to the vertical displacement of the pantograph and the OCR, and has nothing to do with the horizontal distance d. This observation is consistent with flexible-catenary results on stagger, the contact-force waveforms overlap for different stagger values (see section 5.2 of the reference [20]), and mapping this to OCR implies that the overlap spacing d has a negligible effect on F_c.

This paper has been accepted for publication in the AEE journal. This is the version, which has not been fully edited and content may change prior to final publication.
Citation information: DOI 10.24425/aee.2026.156806

3. Multi-objective optimization for dynamic performance of anchor joint

3.1. The process of multi-objective optimization

Figure 5 shows the process of multi-objective optimization. First, the design variables and objective functions are determined.

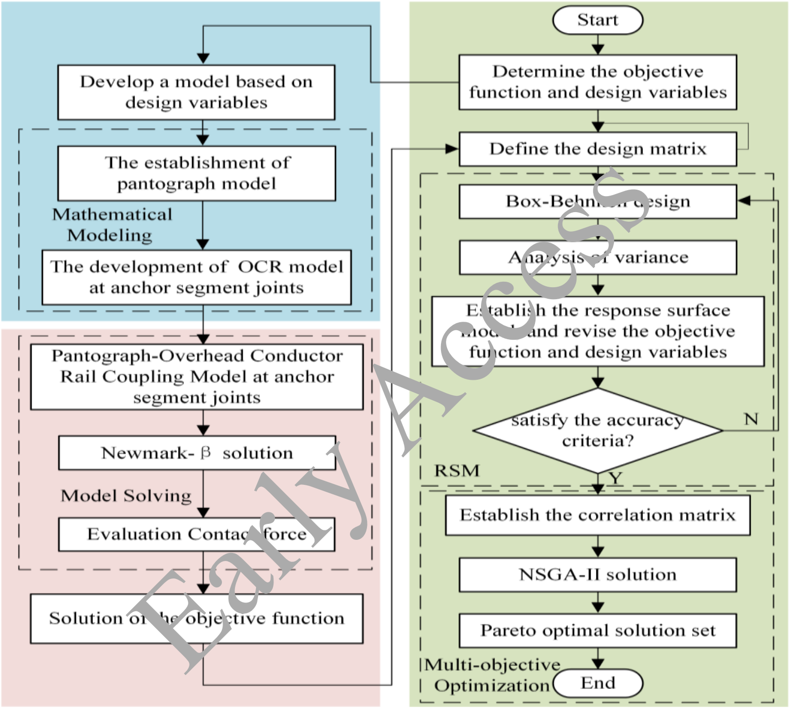

Fig. 5. Multi-objective optimization process

Different parameterized settings are applied to the anchor joint based on the design variables, and the values of the objective functions are calculated. Then, the Box-Behnken Design (BBD) is utilized to conduct a response surface analysis on the design variables. Subsequently, a response surface regression model is constructed based on the data obtained from the Box-Behnken Design. Then, variance analysis is employed to examine the reliability of the constructed response surface regression model [21]. Concurrently, the interactions between each pair of design variables are analyzed through response surface methodology [22]. Finally, the Non-dominated Sorting Genetic Algorithm II (NSGA-II) is used to derive the Pareto optimal solutions located on the Pareto front, in order to determine the optimal parameters under the given constraints.

3.2. Design variables and objective functions

According to previous research by scholars, the length at the anchor point, the bending radius, the cantilever span, and the anchor joint significantly affect the contact force between the POCRS at the anchor joint. Based on the research in reference[11], the standard span of the OCR (x_4) also influences the dynamic performance of the POCRS at the anchor joint. Figure 2 shows a schematic diagram that includes the standard span of the OCR. Single-factor analysis revealed that x_1, x_2, x_3, and x_4 exert the greatest influence on the objective function. Therefore, these four parameters were selected as the design variables and the contact force standard deviation F_δ and the range F_r are chosen as the objective functions. The design variable parameters are shown in Table 3, where –1, 0, and 1 represent the low, medium, and high levels of the design variable parameters, respectively.

3.3. Response surface method

Table 3. Design variable parameter

Parameter	**–1**	**0**	**1**
x_1/(mm)	3	5	7
x_2/(m)	1.2	1.8	2.4
x_3/(m)	5.4	6.6	7.8
x_4/(m)	6	8	10

The response surface method (RSM) is a statistical-based experimental design and data analysis approach used to study the relationships between multiple independent and dependent variables, and to optimize these factors to achieve the best response effect. It mainly includes mathematical and statistical theories such as regression analysis, experimental design, model fitting, and variance analysis [23]. The core of the RSM is to construct a mathematical model to describe the relationship between independent and dependent variables, thereby enabling the input of design variables under constraints to predict the target output of the entire system. The experimental design significantly affects the fitting of the response surface, and variance analysis is used to assess the accuracy of the model. In this paper, response surface analysis with the Box-Behnken experimental design is adopted to analyze whether different design variables have a significant impact on the corresponding responses.

On this basis, Table 3 lists the Box-Behnken experimental design matrix, as shown in Table 4. The numerical simulation and calculation were performed according to the parameters corresponding to this design scheme using the calculation method of the above model, and the results in Table 4 were obtained.

This paper has been accepted for publication in the AEE journal. This is the version, which has not been fully edited and content may change prior to final publication.
Citation information: DOI 10.24425/aee.2026.156806

Table 4. Results of BBD design

Run	***x_1*/(mm)**	***x_2*/(m)**	***x_3*/(m)**	***x_4*/(m)**	***F_δ* /(N)**	***F_r* /(N)**
1	5	1.8	7.8	6	15.936	145.368
2	5	1.2	5.4	8	18.229	141.149
3	5	2.4	7.8	8	18.364	169.185
4	5	2.4	6.6	10	17.862	158.577
5	3	2.4	6.6	8	21.973	206.864
6	7	1.2	6.6	8	14.243	131.19
7	7	1.8	6.6	6	11.199	107.191
8	5	1.8	6.6	8	18.894	167.917
9	3	1.8	7.8	8	22.455	205.52
10	5	1.8	6.6	8	18.79	168.12
11	5	2.4	6.6	6	15.458	140.968
12	7	1.8	7.8	8	14.5	125.767
13	5	1.8	6.6	8	18.972	166.255
14	7	1.8	6.6	10	13.024	106.012
15	7	2.4	6.6	8	14.209	127.5
16	3	1.8	6.6	6	20.402	186.771
17	5	1.2	6.6	6	16.166	154.149
18	5	2.4	5.4	8	18.029	142.596
19	5	1.8	7.8	10	17.197	144.213
20	5	1.2	6.6	10	16.932	141.81
21	5	1.8	5.4	10	17.02	123.356
22	3	1.8	5.4	8	22.25	182.905
23	3	1.2	6.6	8	22.01	210.309
24	7	1.8	5.4	8	14.373	103.152
25	3	1.8	6.6	10	21.04	186.012
26	5	1.8	5.4	6	15.729	125.199
27	5	1.2	7.8	8	18.396	162.817

This paper has been accepted for publication in the AEE journal. This is the version, which has not been fully edited and content may change prior to final publication.
Citation information: DOI 10.24425/aee.2026.156806

4. Results and discussion

4.1. Response surface regression model

Drawing on the outcomes of the Box-Behnken experimental design, a quadratic regression model was employed to fit the response surface models between the objective functions F_δ and F_r and the design variables x_1, x_2, x_3, and x_4, as shown in Eqs. (13) and (14).

Here, x_1, x_2, x_3, and x_4 correspond to the elevation of the first suspension point, the cantilever span, the anchor joint, and the standard span, respectively, while x_1, x_2 and x_1^2 represent the cross terms and quadratic terms of the respective parameters.

$$F_\delta = -12.5561 - 1.66x_1 + 0.2502x_2 + 2.4476x_3 + 7.6813x_4 + 0.0006x_1x_2$$
$$-0.0081x_1x_3 + 0.0742x_1x_4 + 0.0583x_2x_3 + 0.3413x_2x_4 - 0.0031x_3x_4 - 0.0905x_1^2$$
$$-0.9388x_2^2 - 0.182x_3^2 - 0.5191x_4^2. \qquad (13)$$

Here, x_1, x_2, x_3, and x_4 correspond to the elevation of the first suspension point, the cantilever span, the anchor joint, and the standard span, respectively, while x_1, x_2 and x_1^2 represent the cross terms and quadratic terms of the respective parameters.

$$F_r = -416.8584 + 18.9713x_1 - 67.7421x_2 + 131.6968x_3 + 69.226x_4$$
$$-0.051x_1x_2 + 0x_1x_3 - 0.0263x_1x_4 + 1.7087x_2x_3 + 6.2392x_2x_4$$
$$+0.0717x_3x_4 - 0.0626x_1^2 + 2.0533x_2^2 - 9.5458x_3^2 - 5.049x_4^2. \qquad (14)$$

The obtained response surface regression model can predict the maximum values of F_δ and F_r. Figure 6 describes the actual values, predicted values, and contour lines of F_δ and F_r in the fitted model. Figure 6. also includes two asymptotes, $y = 0.95x$ and $y = 1.05x$, and it can be seen that all fitted models fall between these two asymptotes, and the greatest discrepancy between the actual and predicted values of F_δ is 2.78%, and the greatest discrepancy between the actual and predicted values of F_r is 2.42%. The results indicate that the predicted values are close to the actual values, suggesting that the established regression model has a high degree of accuracy.

Meanwhile, the R^2 values of the two subplots in Fig. 6 are 0.9969 and 0.9976, respectively, both of which are very close to 1, indicating that the prediction model has a very high prediction accuracy for F_δ and F_r. Using the asymptotes $y = 1.05x$ and $y = 0.95x$ as reference lines, it can be seen that all prediction points fall between these two lines, which also indicates that the deviation between the predicted values and the actual values is small.

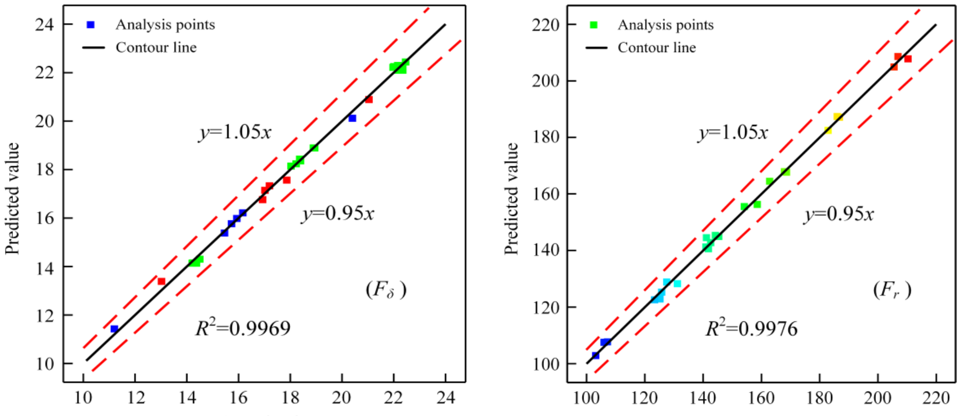

Fig. 6. Comparison of actual and predicted values in fitted model

4.2. Response surface analysis

To verify whether the established response surface model can be used for subsequent optimization design, its accuracy needs to be tested. Therefore, this paper conducts a variance analysis on the fitted models for F_δ and F_r.

The coefficient of determination R^2 is used to assess the overall goodness-of-fit of the regression model; the closer its value is to 1, the better the model fits the data. R^2(Predicted) and R^2(Adjusted) represent the predictive coefficient of determination and the adjusted coefficient of determination, respectively. A discrepancy of less than 0.2 between the two indicates that the quadratic polynomial model possesses a high level of fitting precision. The greater the F-value and the lower the P-value, the more significant the impact of the parameter factor. If the P-value is less than 0.05, then the model term has practical reference value.

The variance analysis results for F_δ and F_r are shown in Tables 5 and 6, respectively. According to the data in Table 5, the response surface model for F_δ is valid, and the parameters x_1, x_4, x_{14}, x_{24}, x_1^2,x_2^2, x_3^2 and x_4^2 in the model are all significant factors affecting the response of F_δ.

Table 5. Variance analysis of F_δ

Size	Quadratic sum	Mean difference	F-value	P-value
Model	228.11	16.29	277.49	< 0.0001
x_1	196.68	196.68	3 349.68	< 0.0001
x_2	0.0005	0.0005	0.0093	0.9247
x_3	0.1236	0.1236	2.11	0.1724

This paper has been accepted for publication in the AEE journal. This is the version, which has not been fully edited and content may change prior to final publication.
Citation information: DOI 10.24425/aee.2026.156806

x_4	5.58	5.58	95.08	< 0.0001
x_1x_2	2.25E-06	2.25E-06	0	0.9952
x_1x_3	0.0015	0.0015	0.0259	0.8748
x_1x_4	0.3522	0.3522	6	0.0306
x_2x_3	0.0071	0.0071	0.1202	0.7349
x_2x_4	0.6708	0.6708	11.42	0.0055
x_3x_4	0.0002	0.0002	0.0038	0.9517
x_1^2	0.6992	0.6992	11.91	0.0048
x_2^2	0.6092	0.6092	10.37	0.0073
x_3^2	0.3633	0.3633	6.24	0.028
x_4^2	22.99	22.99	391.54	< 0.0001

Table 6. Variance analysis of F_r

Size	**Quadratic sum**	**Mean difference**	**F-value**	**P-value**
Model	24 033.27	1 716.66	354.76	< 0.0001
x_1	19 006.01	19 006.01	39 27.73	< 0.0001
x_2	1.52	1.52	0.3134	0.5859
x_3	1 507.81	1 507.81	311.6	< 0.0001
x_4	0.0093	0.0093	0.0019	0.9658
x_1x_2	0.015	0.015	0.0031	0.9565
x_1x_3	0	0	0	1
x_1x_4	0.0441	0.0441	0.0091	0.9255
x_2x_3	6.05	6.05	1.25	0.2852
x_2x_4	224.22	224.22	46.34	< 0.0001
x_3x_4	0.1183	0.1183	0.0245	0.8783
x_1^2	0.3339	0.3339	0.069	0.7973
x_2^2	2.92	2.92	0.6034	0.4523
x_3^2	1 007.74	1 007.74	208.26	< 0.0001
x_4^2	2 175.37	2 175.37	449.56	< 0.0001

From Table 6, it can be observed that the response surface model for F_r is also valid, and the parameters x_1, x_3, x_2, x_4, x_3^2 and x_4^2 in the model are all significant factors affecting the response of F_r.

Table 7 presents the correlation coefficients of the fitted models, where the correlation coefficients R^2 for F_δ and F_r are 99.69% and 99.76%, respectively. Additionally, the differences between R^2(Predicted) and R^2(Adjusted) for F_δ and F_r are 0.011 and 0.0087, respectively, both of which are significantly less than 0.2. These results indicate that the fitted quadratic regression model has a high degree of correlation and is capable of effectively accommodating overall variations.

Figure 7 and Fig. 8 use response surfaces to illustrate the variations of F_δ and F_r with different design variables. Each figure includes the interactions between pairs of design variables on F_δ and F_r. This helps to evaluate the effects of design variables and interaction terms on the response variables.

Figures 7(a)–(c) illustrate the interaction effects of the elevation of the first suspension point with other design variables on F_δ. As x_1 increases, F_δ significantly decreases. However, the variation of x_2 and x_3 has a minimal effect on F_δ. When x_4 increases, F_δ first increases and then decreases. When x_1 is 3.02 mm and x_3 is 6.95 m, F_δ reaches its maximum value of approximately 22.6 N. Obviously, the main reason why F_δ decreases with the increase in x_1 is that the excessive elevation of the suspension point changes the geometric relationship between the POCR, leading to unstable contact with the POCR, and thus decreasing F_δ. Figures 7(d)–(f) illustrate the interaction effects of the cantilever span with the anchor joint span and the standard span on F_δ. It can be observed that as x_3 increases, F_δ also increases. Meanwhile, as x_4 increases, F_δ exhibits an initial rise followed by a subsequent decline. When x_3 is 6.75 m and x_4 is 8.18 m, F_δ reaches its maximum value of approximately 18.96 N.

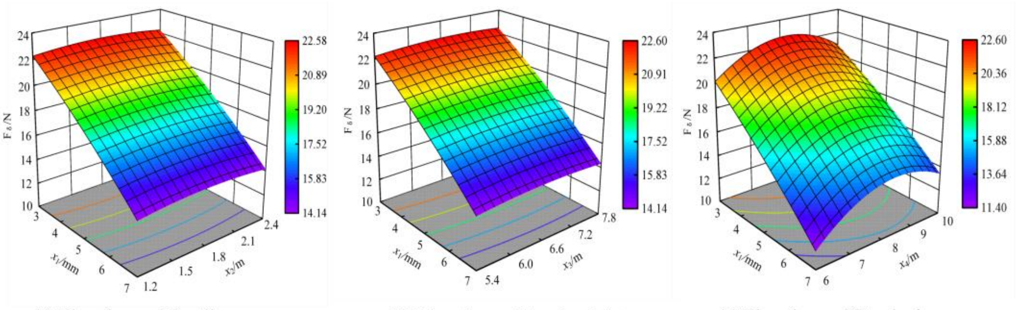

(a) Elevation and Cantilever span (b) Elevation and Anchor joint (c) Elevation and Standard span

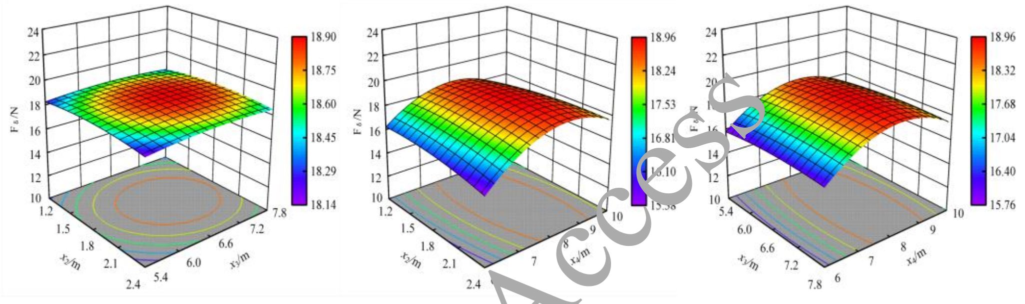

(d) Cantilever span and Anchor joint (e) Cantilever span and Standard span (f) Anchor joint and Standard span

Fig. 7. Response surface of interaction parameter for F_δ

Figures 8(a)–(c) show the interaction effects of the elevation of the first suspension point with other design variables on F_r. When x_1 increases, F_r greatly plunges. The variation of x_2 has almost no effect on F_r. The effects of x_3 and x_4 on F_r are the same, both initially increasing and then decreasing. When x_1 is 3 mm and x_3 is 6.92 m, F_r reaches its maximum value of approximately 210 N, indicating that the risk of POCR disengagement is low at this point. Figures 8(d)–(f) illustrate the interaction effects of the cantilever span with the anchor joint and the standard span on F_r. It can be seen that the raise of x_2 and x_3 exhibits a trend for F_r, first increasing and then decreasing. When x_2 is 2.05 m and x_3 is 7.06 m, F_r reaches its maximum value of approximately 171.9 N. In addition, as x_3 increases from 5.4 m to 7.15 m, F_r increases from 142.59 N to 167.91 N.

This paper has been accepted for publication in the AEE journal. This is the version, which has not been fully edited and content may change prior to final publication.
Citation information: DOI 10.24425/aee.2026.156806

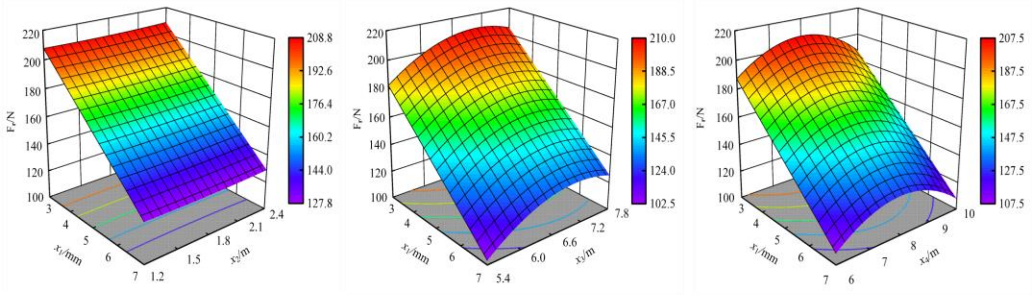

(a) Elevation and Cantilever span (b) Elevation and Anchor joint (c) Elevation and Standard span

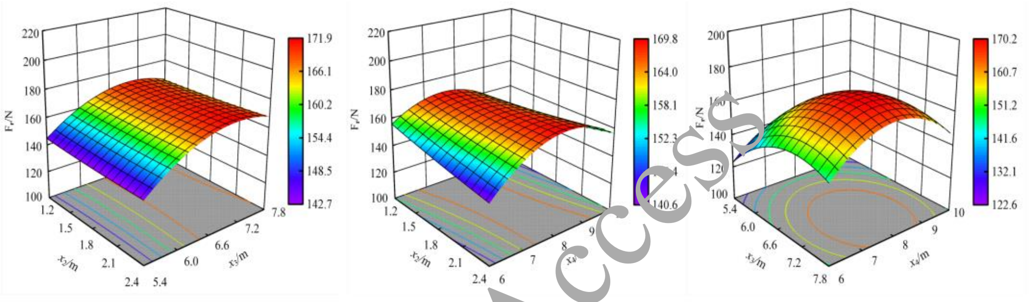

(d) Cantilever span and Anchor joint (e) Cantilever span and Standard span (f) Anchor joint and Standard span

Fig. 8. Response surface of interaction parameter for F_r

Table 7. The correlation coefficient of the fitted model

Fitted model	F_δ	F_r
R^2	0.9969	0.9976
R^2 (Predicted)	0.9823	0.9861
R^2 (Adjusted)	0.9933	0.9948

4.3. NSGA-II optimization

To derive the mutual influence patterns of x_1, x_2, x_3, and x_4 on F_δ and F_r, the response surface regression mathematical model established above is used, and the Non-dominated Sorting Genetic Algorithm II (NSGA-II) is adopted as the optimization algorithm for F_δ and F_r.

NSGA-II employs a fast non-dominated sorting algorithm, and introduces the concept of crowding distance. Its advantages lie in effectively reducing computational complexity, preventing the loss of superior solutions during the selection process, and ensuring a uniform distribution of the solution set in the objective space.

Figure 9. depicts the process diagram of the NSGA-II, and the basic procedure of the NSGA-II algorithm is as follows:

Step 1: First, initialize the population and set the generation number Gen to 1.

This paper has been accepted for publication in the AEE journal. This is the version, which has not been fully edited and content may change prior to final publication.
Citation information: DOI 10.24425/aee.2026.156806

Step 2: Calculate the quadratic regression function obtained from the response surface, perform non-dominated sorting and crowding distance calculation, and then generate the offspring population through crossover and mutation.

Step 3: Combine the parent and offspring populations for non-dominated sorting and calculate the crowding distance of individuals in the non-dominated layers.

Step 4: Generate a new offspring population through crossover and mutation.

Step 5: Based on the new individuals in the population, use the genetic algorithm to obtain a new population and continue generating until the maximum number of iterations is reached.

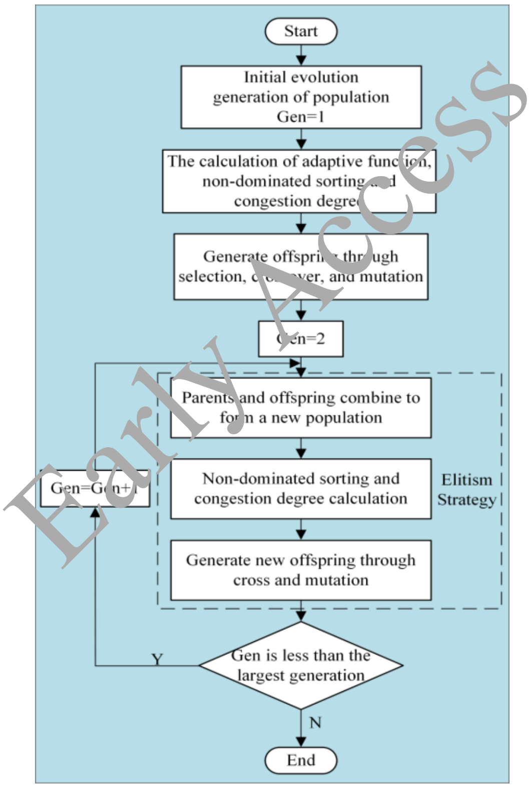

Fig. 9. NSGA-II algorithm flowchart

In the mathematical model for multi-objective optimization, F_δ and F_r are both determined by the aforementioned response surface regression model. In the NSGA-II, the maximum number of iterations is set to 150, the population size is 50, the crossover probability is 0.7, the mutation probability is 0.4, and the mutation rate is 0.02. The iterations are performed in MATLAB to obtain the Pareto optimal front distribution. Figure 10. shows the variation of the

This paper has been accepted for publication in the AEE journal. This is the version, which has not been fully edited and content may change prior to final publication.
Citation information: DOI 10.24425/aee.2026.156806

Pareto optimal front distribution. It is readily apparent that as F_δ increases, F_r decreases, indicating a conflicting relationship between the two; to maximize them simultaneously, an optimal balance point must be sought. From Figs. 10(a) and (b), it can be seen that when the number of iterations is 5 and 20, respectively, the population distribution is chaotic and sparse, and the optimal solution has not been reached. In Figs. 10(c) and (d), when the number of iterations reaches 50, the Pareto front has already formed a set of curve solutions; by 80 iterations, the NSGA-II algorithm continuously optimizes the crowding of the objective functions, making the Pareto front distribution more uniform. Compared to the aforementioned iterative situations, after 150 iterations (Fig. 10(e)), the Pareto front distribution becomes more uniform, indicating that the NSGA-II has converged. The change intervals for F_δ and F_r under the satisfaction of constraints are 22.3 N ≤ F_δ ≤ 22.65 N and 209 N ≤ F_r ≤ 212.5 N.

$$\begin{cases} \text{Maximize: } F_\delta(x_1,x_2,x_3,x_4) \\ \text{Maximize: } F_r(x_1,x_2,x_3,x_4) \\ \text{Where: } F_\delta \geq 11.199\ \text{N} \\ F_r \geq 103.152\ \text{N} \\ 3\ \text{mm} \leq x_1 \leq 7\ \text{mm} \\ 1.2\ \text{m} \leq x_2 \leq 2.4\ \text{m} \\ 5.4\ \text{m} \leq x_3 \leq 7.8\ \text{m} \\ 6\ \text{m} \leq x_4 \leq 10\ \text{m} \end{cases} . \tag{15}$$

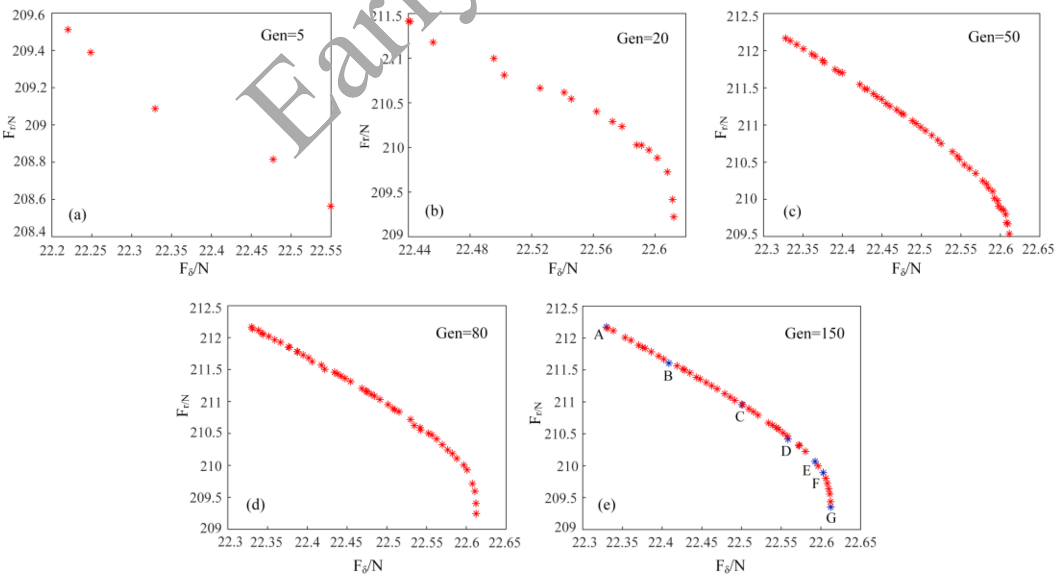

Fig. 10. Evolution of the Pareto front during the iterative process

This paper has been accepted for publication in the AEE journal. This is the version, which has not been fully edited and content may change prior to final publication.
Citation information: DOI 10.24425/aee.2026.156806

From Fig. 10(e), it can be seen that the maximum F_r of 212.17 N and the maximum F_δ of 22.61 N correspond to points A and G, respectively. Compared with the pre-optimization state, for the optimization points B, C, D, E, and F, at least one of the two objective functions F_δ and F_r is better than before optimization. After Pareto optimization, the optimal values of F_δ and F_r and their corresponding structural parameter variables are shown in Table 8. Figure 11 shows the contact force curves of the POCR at points A, B, C, D, E, F and G before and after optimization at the anchor joint. As can be seen from Fig. 11, the contact force fluctuation between the POCR at the anchor joint for optimization point D is smaller than that of the other six optimization points, which means that F_δ and F_r have reached their optimal balance point. Therefore, this paper selects the Pareto solution at point D as the final result of the multi-objective optimization.

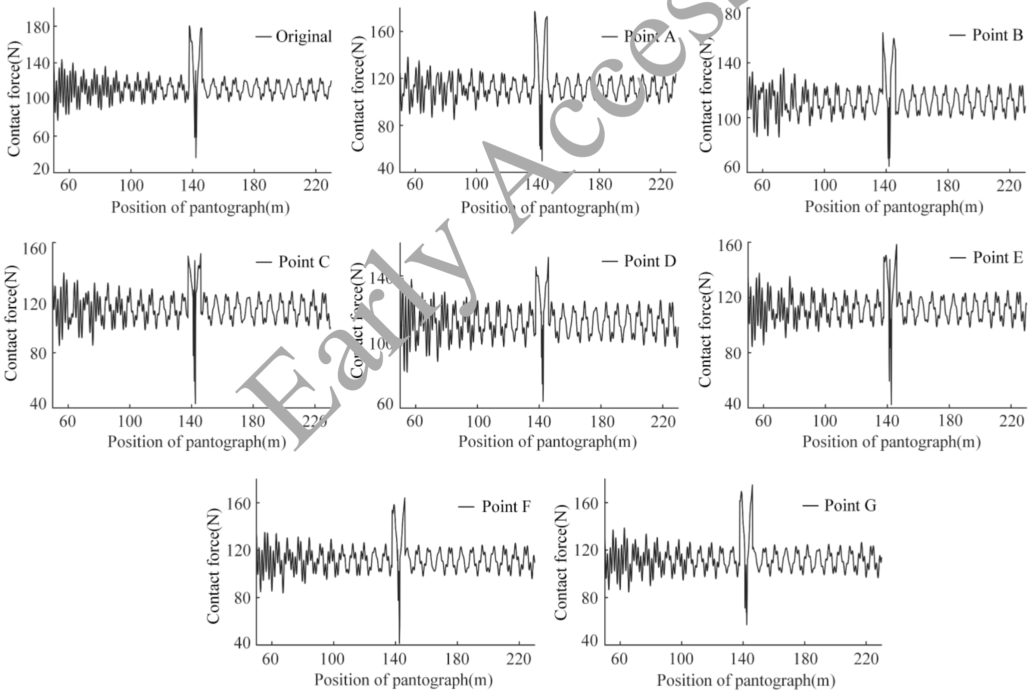

Fig. 11. The contact force curves of each optimization point at the anchor segment joint

Table 8. The structural parameters of each optimization point

Optimization point	x_1**/(mm)**	x_2**/(m)**	x_3**/(m)**	x_4**/(m)**	F_δ**/(N)**	F_r**/(N)**
A	3.24	2.4	7.13	8.36	22.33	212.17

B	3.15	2.31	7.11	8.29	22.41	211.63
C	3.06	2.2	7.08	8.24	22.49	211.03
D	3	2.06	7.09	8.23	22.56	210.42
E	3.05	1.97	7.02	8.21	22.59	210.02
F	3.11	1.87	6.95	8.2	22.6	209.53
G	3.18	1.84	6.87	8.18	22.61	209.36

4.4. Numerical optimization results analysis

To validate the effectiveness of the NSGA-II–derived Pareto-optimal solution (point D), we benchmarked it against three methods: the pre-optimization baseline (Original), the optimum from the Box–Behnken design, and the optimum from the Non-Dominated Sorting Dung Beetle Optimization (NSDBO) algorithm. Parameter comparisons between point D and the two method optima are given in Table 9, while Fig. 12(a) contrasts their simulated responses; Fig. 12(b) reports contact force statistics across all four scenarios. Overall, the NSGA-II solution delivers the most balanced and effective trade-off, outperforming both Box–Behnken and NSDBO on key evaluation criteria and yielding more stable contact forces than the baseline (Original). The maximum discrepancy between the NSGA-II Pareto solution and the numerical results is 16.55% (within 20%), confirming the reliability of the NSGA-II outcome.

Table 9. Comparison of anchor segment joint parameters before and after optimization

Scheme	**x_1/(mm)**	**x_2/(m)**	**x_3/(m)**	**x_4/(m)**	**F_δ/(N)**	**F_r/(N)**
Original	4	1.2	5.4	10	20.29	155.81
Box-Behnken	3.4	1.81	7.01	8.12	21.54	196.74
NSGA-II	3	2.06	7.09	8.23	22.56	210.42
NSDBO	3.2	2.11	7.05	8.21	21.98	194.96

In Fig. 12(a), it can be seen that the fluctuation range of the POCR contact force corresponding to the anchor joint parameters obtained through the NSGA-II is significantly reduced compared with those obtained through the Box-Behnken experimental design and Original. $F_{\max}$ decreases from 180.49 N to 151.31 N, while $F_{\min}$ increases from 36.3 N to 64.04 N. F_δ is raised by 11.18%, and F_r is increased by 35.04% compared with Original. Meanwhile, compared with the NSDBO algorithm, F_δ is increased by 2.64% and F_r is raised by 7.35%. This further demonstrates the effectiveness of the NSGA-II algorithm.

This paper has been accepted for publication in the AEE journal. This is the version, which has not been fully edited and content may change prior to final publication.
Citation information: DOI 10.24425/aee.2026.156806

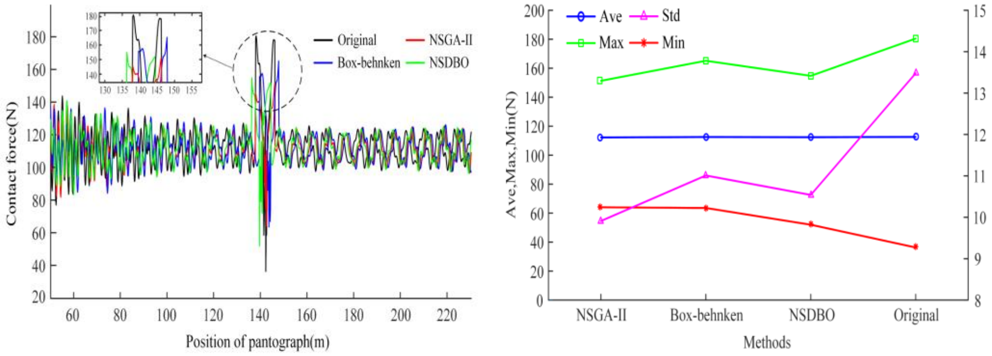

Fig. 12. (a) Comparison of the contact force with four methods; (b) the statistics of contact force

The dynamic simulation results of four different methods are shown in Fig. 12(b), and the statistical values are presented in Table 10. It can be observed that the maximum values and standard deviations of the contact force obtained by the NSGA-II and NSDBO algorithms have significantly decreased, with the maximum values reduced by 16.17% and 14.26%, respectively, and the standard deviations reduced by 26.48% and 21.81%, respectively, leading to noticeable improvements in F_{δ} and F_r. The minimum values of the contact force obtained by the NSGA-II algorithm and the Box-Behnken experimental design have significantly increased, with the minimum values increased by 76.41% and 75.09%, respectively, effectively reducing the occurrence of pantograph-catenary separation. The average contact force has hardly changed at all. In summary, the NSGA-II is superior to other methods.

Table 10. Statistical characteristic values

Method	**Ave (N)**	**Std (N)**	**Max (N)**	**Min (N)**
Original	112.59	13.48	180.49	36.3
Box-Behnken	112.52	11.01	165.16	63.56
NSDBO	112.41	10.54	154.74	52.01
NSGA-II	112.24	9.91	151.31	64.04

5. Conclusion

This paper establishes an RSM-NSGA-II optimization model for the anchor joint, which is used for multi-objective optimization of the dynamic performance at the anchor joint. The design variables include x_1, x_2, x_3, and x_4, while the optimization variables are F_δ and F_r. A regression model for the optimization variables was established based on the RSM. The Pareto front was obtained using the NSGA-II, and seven balanced points on the Pareto front were selected for numerical simulation and comparison. The optimal point was then chosen from these points. The following conclusions were drawn:

1) A mathematical model between the anchor joint parameters and the objective functions was established using the Box-Behnken response surface experimental design. The model was validated by using the coefficients of R^2, R^2 (Predicted), and R^2 (Adjusted), which are close to 1, and by conducting an analysis of variance (ANOVA) test. The established regression model was proven to have high precision and the ability to well adapt to the overall trend of changes.
2) The effects of x_1, x_2, x_3, and x_4 on the dynamic performance at the anchor joint were investigated. As x_1 increases, F_δ significantly decreases, while their effect on F_r is similar. When x_1 increases from 3 mm to 7 mm, F_δ decreases from 22.6 N to 11.4 N. The variation of x_2 and x_3 has a minimal effect on F_δ. When x_4 = 8.23 m, the maximum F_δ is 22.46 N. When x_2 increases from 1.2 m to 2.4 m, F_r hardly changes. When x_3 is 7.1, F_δ is 20.46% higher than when x_3 is 5.4. When x_4 = 8.21 m, the maximum F_r is 206.31 N. The results indicate that x_1 has the greatest impact on F_δ, while x_1 and x_4 has the significant influence on F_r.
3) The multi-objective optimization of the established response surface regression model was performed using the NSGA-II algorithm. F_δ and F_r are two conflicting functions, and there are different trade-offs between them. When F_δ increases, F_r decreases, and vice versa, thus forming a Pareto optimal solution set.
4) Based on the multi-objective optimization Pareto front, seven balanced points on the Pareto front were selected for numerical simulation and comparison, point D was determined to be the optimal solution. Additionally, to further demonstrate the effectiveness of the NSGA-II algorithm, the Box-Behnken experimental design and the NSDBO algorithm were introduced for comparison. Compared to these two methods, the NSGA-II algorithm increased F_δ by 4.73% and 2.64%, respectively, and increased F_r by 6.95% and 7.93%, respectively. The dynamic performance at the anchor joint is optimal when x_1 is 3 mm, x_2 is 2.06 m, x_3 is 7.09 m, and x_4 is 8.23 m. Compared with the original design, the optimized F_δ increased by 11.18%, and F_r was raised by 35.04%.

References

[1] Gregori S., Gil J., Tur M., Tarancón J.E., Fuenmayor F.J., *Analysis of the overlap section in a high-speed railway catenary by means of numerical simulations*, Engineering Structures, vol. 221, no. 110963 (2020), DOI: 10.1016/j.engstruct.2020.110963.

This paper has been accepted for publication in the AEE journal. This is the version, which has not been fully edited and content may change prior to final publication.
Citation information: DOI 10.24425/aee.2026.156806

[2] Song Y., Zhang M.J., Oseth O., Ronnquist A., *Wind deflection analysis of railway catenary under crosswind based on nonlinear finite element model and wind tunnel test*, Mechanism and Machine Theory, vol. 168, no. 104608 (2022), DOI: 10.1016/j.mechmachtheory.2021.104608.

[3] Song Y., Liu Z.G., Wang H.R., Lu X.B., Zhang J., *Nonlinear analysis of wind-induced vibration of high-speed railway catenary and its influence on pantograph-catenary interaction*, Veh. Syst. Dyn., vol. 54, no. 6, pp. 723–747 (2016), DOI: 10.1080/00423114.2016.1156134.

[4] Bautista A., Montesinos J., Pintado P., *Dynamic interaction between pantograph and rigid overhead lines using a coupled FEM — multibody procedure*, Mechanism and Machine Theory, vol. 97, pp. 100–111 (2016), DOI: 10.1016/j.mechmachtheory.2015.10.009.

[5] Chen L., Duan F., Song Y., Hu Z., Liu Z., *Three-dimensional contact formulation for assessment of dynamic interaction of pantograph and overhead conductor rail system*, Vehicle System Dynamics, vol. 61, no. 9, pp. 2432–2455 (2022), DOI: 10.1080/00423114.2022.2112607.

[6] Hu Z.Y., Song Y., Chen L., Duan F.C., Liu Z.G., Feng X.H., *Experimental and Numerical Exploration of Support Stiffness Influence on the Current Collection Quality of Pantograph and Overhead Conductor Rail System*, IEEE Trans. Transp. Electrif., vol. 10, no. 3, pp. 7112–7126 (2024), DOI: 10.1109/tte.2023.3345955.

[7] Song Y., Liu Z.G., Ronnquist A., Nåvik P., Liu Z.D., *Contact Wire Irregularity Stochastics and Effect on High-Speed Railway Pantograph-Catenary Interactions*, IEEE Trans. Instrum. Meas., vol. 69, no. 10, pp. 8196–8206 (2020), DOI: 10.1109/tim.2020.2987457.

[8] Mak M.K., *Adoption of Overhead Rigid Conductor Rail System in MTR Extensions*, Journal of International Council on Electrical Engineering, vol. 2, no. 4, pp. 463–466 (2014), DOI: 10.5370/jicee.2012.2.4.463.

[9] Vera C., Suarez B., Paulin J., Rodríguez P., *Simulation model for the study of overhead rail current collector systems dynamics, focused on the design of a new conductor rail*, Veh. Syst. Dyn., vol. 44, no. 8, pp. 595–614 (2006), DOI: 10.1080/00423110500165499.

[10] Song Y., Rønnquist A., Jiang T., Nåvik P., *Railway pantograph-catenary interaction performance in an overlap section: Modelling, validation and analysis*, Journal of Sound and Vibration, vol. 548 (2023), DOI: 10.1016/j.jsv.2022.117506.

[11] Yao Y.M., Yang Z.P., Wang J., Zhang W.X., *Analysis of contact force and uplift of pantograph-catenary system in overlap section based on numerical simulations and experimental tests*, Veh. Syst. Dyn., vol. 61, no. 10, pp. 2492–2515 (2022), DOI: 10.1080/00423114.2022.2117056.

[12] Simarro M., Postigo S., Prado-Novoa M., Pérez-Blanca A., Castillo J.J., *Analysis of contact forces between the pantograph and the overhead conductor rail using a validated finite element model*, Engineering Structures, vol. 225, no. 111265 (2020), DOI: 10.1016/j.engstruct.2020.111265.

[13] Rahman Y.A., Manjang S., Yusran Y., Ilham A.A., *Distributed generation's integration planning involving growth load models by means of genetic algorithm*, Archives of Electrical Engineering, vol. 67, no. 3, pp. 667–682 (2018), DOI: 10.24425/123671.

[14] Knypiński L., Devarapalli R., Le Menach Y., *Constrained optimization of the brushless DC motor using the salp swarm algorithm*, Archives of Electrical Engineering, vol. 71, no. 3, pp. 775–787 (2022), DOI: 10.24425/aee.2022.141684.

This paper has been accepted for publication in the AEE journal. This is the version, which has not been fully edited and content may change prior to final publication.
Citation information: DOI 10.24425/aee.2026.156806

[15] Zhao S., Pattanadech N., *Power transformer fault warning combining support vector machine and improved grey wolf optimization algorithm*, Archives of Electrical Engineering, vol. 74, no. 1, pp. 191–208 (2025), DOI: 10.24425/aee.2025.153019.

[16] Ferreira S.L.C. *et al*., *Box-Behnken design: an alternative for the optimization of analytical methods*, Analytica Chimica Acta, vol. 597, no. 2, pp. 179–186 (2007), DOI: 10.1016/j.aca.2007.07.011.

[17] EN50367, *Railway applications - Fixed installations and rolling stock - Criteria to achieve technical compatibility between pantographs and overhead contact line*, Ratified European Text (2020).

[18] TB/T 3271, *Railway applications-Current collection systems-Technical criteria for the interaction between pantograph and overhead line*, China Railway Industry Standard (2011).

[19] Lee K., Cho Y., Chung J., *Dynamic contact analysis of a tensioned beam with a moving mass–spring system*, Journal of Sound and Vibration, vol. 331, no. 11, pp. 2520–2531 (2012), DOI: 10.1016/j.jsv.2012.01.014.

[20] Wang Y., He Y.K., Zhao G.H., Chen X.Q., Ge L.J., Ma A.P., *Improved Shape-Finding Modeling and Dynamic Performance Analysis of Electrified Railway Pantograph-Catenary Coupling System in Noncrossing Turnout Section*, IEEE Transactions on Instrumentation and Measurement, vol. 74, no. 3540310 (2025), DOI: 10.1109/tim.2025.3571158.

[21] Sharma J., Sharma G.K., Varma T., Boolchandani D., *Optimization of Performance Parameters of Phase Frequency Detector Using Taguchi DoE and Pareto ANOVA Techniques*, J. Circuits Syst. Comput., vol. 32, no. 9 (2023), DOI: 10.1142/s021812662350158x.

[22] Chen W.H., Chang C.M., Mutuku J.K., Lam S.S., Lee W.J., *Analysis of microparticle deposition in the human lung by taguchi method and response surface methodology*, Environ. Res., vol. 197, no. 110975 (2021), DOI: 10.1016/j.envres.2021.110975.

[23] Li Z.P., Lu D.G., Gao X.J., *Optimization of mixture proportions by statistical experimental design using response surface method - A review*, J. Build. Eng., vol. 36, no. 102101 (2021), DOI: 10.1016/j.jobe.2020.102101.